Beam Diagnostics for Medical Accelerator

Tomasz Cybulski[#], Carsten Peter Welsch
University of Liverpool, Department of Physics, LiverpoolL69 7ZE, UK
Cockcroft Institute, Daresbury, Warrington WA4 4AD, UK

Dose-delivered monitoring plays a vital role in proton radiotherapy. At present, the on-line dose records are based on readings from ionisation chambers, which serve as a gold standard in clinical dosimetry. A new non-invasive method for dose on-line monitoring is under development based on a silicon multi-strip detector LHCb VELO (VErtex LOcator), operating at the LHCb experiment at CERN. The proposed method relies on the proton beam 'halo' measurements related to the absolute beam current measurement provided by a Faraday cup (FC). A FC optimisation study was performed for assuring the high precision of the measurement by matching the beam stopper charge collection efficiency to the beam properties at the Clatterbridge Centre for Oncology (CCO), where initial proof of principle measurements will be performed. The above-mentioned method is described in this paper and accompanied by the results of the FC optimisation.

I. INTRODUCTION

Modern medicine takes advantage of different treatment techniques to fight against malicious cancer cells. Apart from classical methods, such as tumour resection or chemotherapy, radiotherapy techniques offer a very precise treatment tool. This tool can be used on its own or complementary to, for example, chemotherapy. The discovery of X-rays by Wilhelm Conrad Roentgen in 1894 started an era where ionising radiation found its applications in both industry and medicine. Linear accelerators (LINAC) became a source of electron and X-ray photon beams of energies higher than 1MeV [2].

Electron beams and X-ray photons of energies varying between 5 and 16 MeV are most commonly used in cancer treatment [1]. The development of LINACs has made them easy to use, user friendly and compact facilities. The standardised technology has also influenced the price by reducing the cost and making it affordable to radiotherapy centres all over the world. Availability of the technique resulted also in the standardisation of the medical procedures. Other disciplines such as dosimetry and radiobiology developed from this technology, resulting in a detailed assessment of all the pros and cons of the applied methods [1]. Photons and electrons interactions with live tissue result in the ionisation of cell structures independent of the type; cancer-affected or healthy tissue. Thus, attention is turned to mitigate the damage probability to healthy tissue surrounding the tumour. Key requirements are indentified as more conscious radiation application, precise beam parameters and dose control (energy, geometrical extent), as well as looking for more precise tool for deposited energy monitoring (absorbed dose). Ultimately, protons and heavy ions demonstrate very advantageous dose distribution profiles, in comparison to photons or electrons.

Heavy charged particles' dose depth profiles differ significantly from photons. They show an inverted dose profile with a prominent peak at the end of their range, the so called Bragg peak. Protons entering matter undergo multiple Coulomb interactions, decreasing their kinetic energy [5, 9]. The energy transfer is approximately inversely proportional to the particle velocity squared and results in an increased dose, where protons come to rest. For over two decades 62 MeV proton beams have been used at the Clatterbridge Centre for Oncology (CCO) for eye cancer therapy. The dose-delivered control during treatment is based on a stack of parallel – plate ionisation chambers [6]. A new non-interceptive monitor for both online dose recording and accelerator quality assurance is described in this paper. It makes use of the LHCb VErtex Locator detector (VELO) and a dedicated Faraday cup (FC). Whilst the proton beam 'halo' will be monitored by the LHCb VELO detector, the

FC will be periodically used to relate the 'halo' readings to the absolute beam current and will thus serve as a constancy check monitor.

II. RESOURCES AND METHOD

A. Accelerator

The experimental set – up is being prepared to be integrated in the ocular treatment beam line at CCO, where the Scanditronix MC-60 PF cyclotron has been continuously delivering proton beam for the eye cancer treatment since 1989. The treatment beam line is an 'in-house' built passive scattering system, based on a combination of two W scattering foils positioned at the end of the vacuum beam tube. [6]

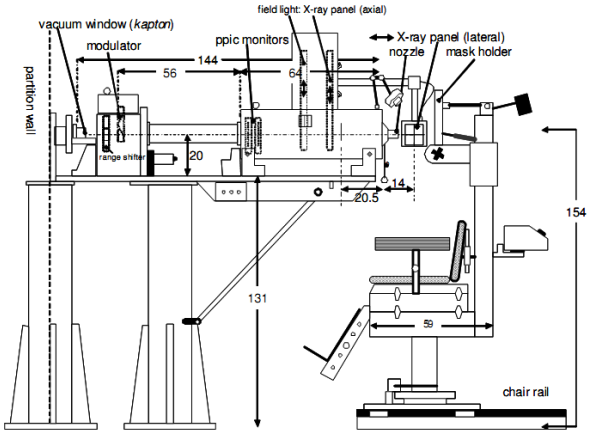

FIG. 1. Outline of the CCO proton therapy beam line. [6]

The foil thickness was selected to be 25 µm and constitutes an optimum between beam lateral spread and proton energy loss. A range shifter and a beam modulator are installed downstream from the vacuum window. The last section of the treatment line between the modulator and the treatment isocentre is a 1.34 m long drift space in air, see FIG.1. Therefore, various interactions with air molecules decrease the maximum beam energy to approx. 60 MeV and widen lateral profile.

The Scanditronix MC-60 PF cyclotron is a first harmonic mode operating machine dedicated to proton acceleration. This isochronous accelerator is fitted with two accelerating cavities of a width of 90 RF degrees and a Penning Ion Gauge [7] as an ion source located in its centre. The accelerator technical specification and calculated beam characteristics are summarized in TABLE I.

TABLE I. Scanditronix MC60-PF Cyclotron technical specification and calculated beam time structure.

Ion max. kinetic energy [MeV]	62.0
Ion type	p
Magnetic field avg. min [T]	1.05
Magnetic field avg. max. [T]	1.75
Magnetic field max. hill [T]	2.13
RF frequency [MHz]	26.7
RF period [ns]	37.5
RF beam acceptance [deg]	13
Treatment beam current [nA]	5.0
Number of ions [ions / s]	$3.12 \cdot 10^{+10}$
Number of ions per bunch	$1.17 \cdot 10^{+3}$
PIG source current [µA]	$1.38 \cdot 10^{-1}$
Beam power [W]	0.3
Peak beam power [W]	$1.12 \cdot 10^{-8}$
Energy deposited by bunch [J]	$4.06 \cdot 10^{-10}$

B. Measurement Method

The experimental set-up consists of the LHCb VELO detector serving as a standalone and non–invasive on–line beam current monitor. The LHCb VELO detector was designed to be operated in vacuum. However, experimental constraints at CCO require its operation in air. The first tests are planned to

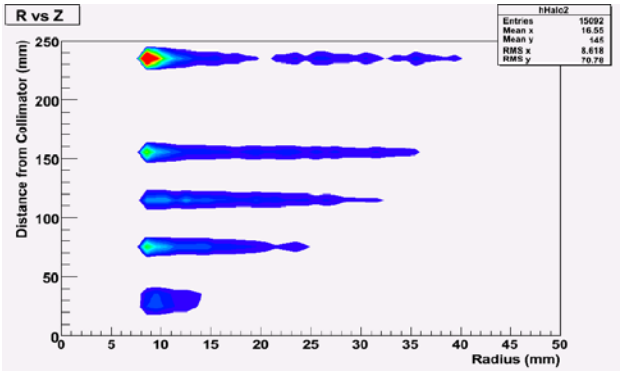

FIG. 2. Proton beam divergence measured by the LHCb VELO detector at five different distances from the final beam collimator (including measurements taken in the isocentre). [2]

integrate the detector directly in a free space region within the treatment beam line, between the modulator and integrated parallel-plate ionisation chambers, see FIG. 3 and FIG. 9. It should be noted that the sensor readout electronics produces a heat load of 40 W. As a result, it was essential to couple the electronics board with a purpose-built cooling system through a Thermo-Pyrolytic-Graphite central base. The cooling down process may, however, lead to water condensation on the detector elements. The major challenge during the

design of a dedicated support structure was, therefore, the integration of an efficient cooling system together with a precision detector positioning system.

The 'halo' region hit rate measured by the VELO detector is going to be related in the next step with the absolute beam current value provided by the FC.

The VELO detector performance as a non–invasive monitor was shown in 2010 when first feasibility tests were performed at the treatment beam line demonstrating the possibility of non–intrusive beam monitoring [8]. These initial measurements consisted of data taken at several points along the propagation direction of the beam, starting from the brass collimator, see FIG. 1. A new method was proposed to relate the proton 'halo' region hit rate, measured by the VELO detector, with the absolute beam current provided by a FC and thereby get an indication of the dose delivered to the patient. Proton beam 'halo' should be understood as halo formed due to particles scattering on air molecules, rather than complex beam 'halo' propagation in the vacuum beam line.

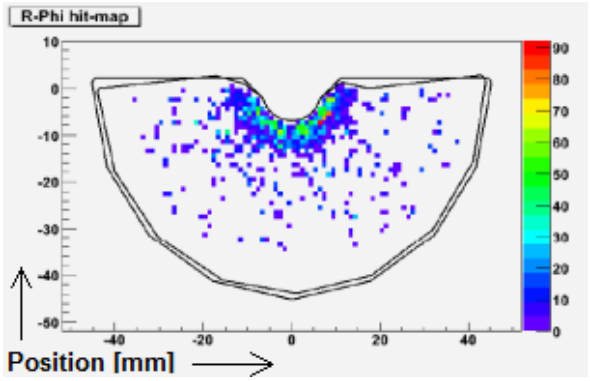

FIG. 3. Proton 'halo' hit map measured by the LHCb VELOS Phi - sensor. The scale on the right hand side of the plot shows the signal strength in ADC counts [2].

For the purpose of this experiment a dedicated stand was designed to integrate the VELO detector with the treatment beam line (to be covered in the following section). In parallel, an optimisation of the FC design was performed to maximise the charge collection efficiency by matching arrangement to the CCO treatment beam parameters. The LHCb VELO detector technology and simulation results of the FC optimisation are presented in this paper.

III. LHCB VELO DETECTOR

The LHCb VErtex LOcator detector constitutes the most essential part of the non-invasive beam diagnostics in the set-up being described. The proton 'halo' intensity distribution measured by the VELO detector will be related to absolute beam current value readings from the FC. Further on, the stand-alone VELO detector operation is meant to provide the user with real-time dose information. This beam current monitoring method does not perturb the beam, which results in neither the beam energy degradation taking place nor widening of the beam profile.

The LHCb VELO detector is a multi-strip silicon detector optimally designed for tracking vertices produced in b-hadrons decays. It plays a double role in the LHCb experiment by providing the system with track coordinates in the vicinity of the collision region and giving input for the second level trigger (L1).

A. The LHCb VELO hybrid

Two semi-circular semiconductor sensors, each composed of 2048 diode stripes, form the detector active area. A stack of the φ - and r – measuring sensors gives the track coordinates in the polar coordinate system and constitutes a detector hybrid, see FIG. 4 and FIG.5.

The semiconductor diodes were manufactured in silicon as n+ – on – n junction (the earlier sensor edition relied on p+ - on – n junction). The technical specification of the sensor architecture can be found in [9]. The r – measuring area is divided into four angular sections, 45 degrees in extent each. The φ – sensor arrangement is more advanced with respect to the r side. The active area is divided into a smaller inner region and a larger outer region, see FIG. 5. Additionally, two stereo angles, with respect to the radius, were introduced to the stripes and consistently set to 20 degrees for inner strips and 10 degrees for outer strips. Moreover, the skew angle is reversed for inner and outer strips, respectively. This arrangement is very advantageous in ghost hit recognition. This happens when two simultaneous hits take place at two different stripe pairs. At that time it is impossible to distinguish hit place, unless

information from two adjacent detector hybrids is provided, see FIG. 4.

The diode readout bonds are arranged radially and guided to the sensor outer circumference. Therefore, the second metal layer was applied to isolate the inner and outer stripes signal paths. The metal layer isolation from the silicon diode stripes is made of 3 µm thick SiO_2 layer.

The semiconductor junction depleting potential is fed through poly-silicon resistors. It can be as high as 500 V when the radiation damage occurs with long irradiation / operation times.

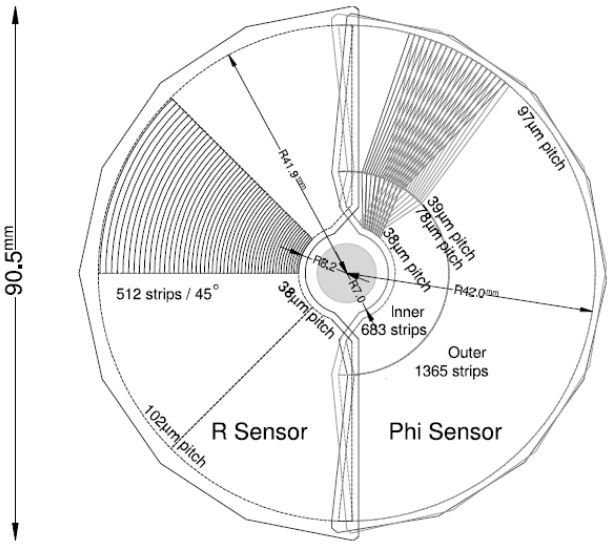

FIG. 4. The LHCb VELO detector hybrid layout: central base of Thermo – Pyrolitic Graphite constitutes a mechanical support for both r- and φ- sensors and readout electronics. [15]

TABLE II. Summary of LHCb VELO sensors design, see also FIG. 5 for reference.

	R sensor	*φ sensor*
Readout channels per sensor	2048	2048
Sensor thickness [µm]	300	300
Smallest pitch [µm]	40	38
Largest pitch [µm]	102	97
Inner radius of active area [mm]	8.2	8.2
Outer radius of active area [mm]	42	42
Angular coverage [deg]	182	~ 182
Stereo angle [deg]	-	10 - 20

The $r\varphi$ geometry of the sensors is beneficial in both keeping low detector/stripes occupancy throughout the detector and holding the detector resolution at the same level across the detection area. Additionally, the calculation algorithm does not require time-consuming calculations in the rectilinear coordinates system.

The rz position reconstruction relays on a fixed distance between the adjacent modules in the experiment. At the CCO the rz position is determined by the position of the longitudinally oriented translation stage, see FIG. 9.

B. Read out electronics

The LHCb VELO detector has been fully designed to comply with the timing of the LHC triggers at 40MHz bunch crossing frequency (L1 trigger). The electronics components are based on CMOS technology.

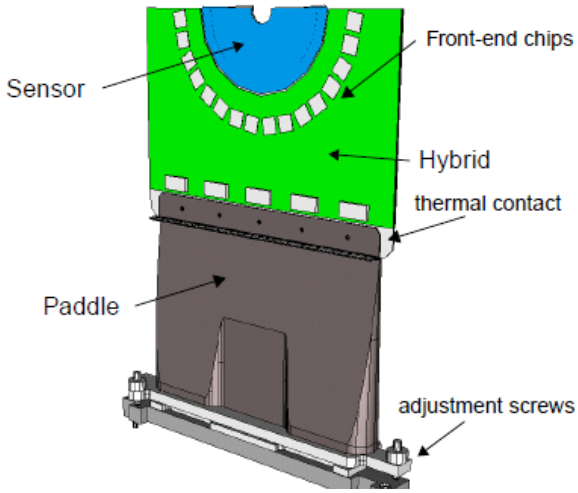

FIG. 5. The LHCb VELO sensors architecture. Phi - measuring sensor provides angular information on the track coordinates and r – sensor provides the measure of radial coordinate. [17]

The space shortage near the reaction region used to be a big constraint for the electronics design. Therefore, the detector readout and signal transfer are analogue to save space. Data acquisition board cards (DAQ) – TELL1, two for each detector hybrid, find themselves in a separate room, far from the interaction region.

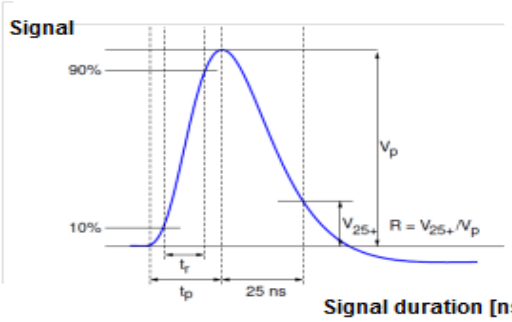

FIG. 6. Beetle chip output pulse shape and its parameters. Vp - peaking potential, R - remainder. [13]

The LHCb VELO schematic readout and control electronics diagram at CERN is

depicted in FIG. 6. Signals from the stripes are routed into 16 custom designed Beetle chips, where data from successive collision events is stored before processing. When the readout decision trigger arrives, the stored charge is guided out from the chips through special Kapton band cables and transferred onto repeater boards, where, for instance, the line equalizer compensates for the signal loss in the 60m long AWG26 Cat5 signal cables. The signal enhancement is performed by active and radiation-hard electronics. The repeater boards also manage triggering timing information for the detector hybrid within the Experiment Control System (ECS). Moreover, they also distribute low and high voltage to power electronic components on the hybrid.

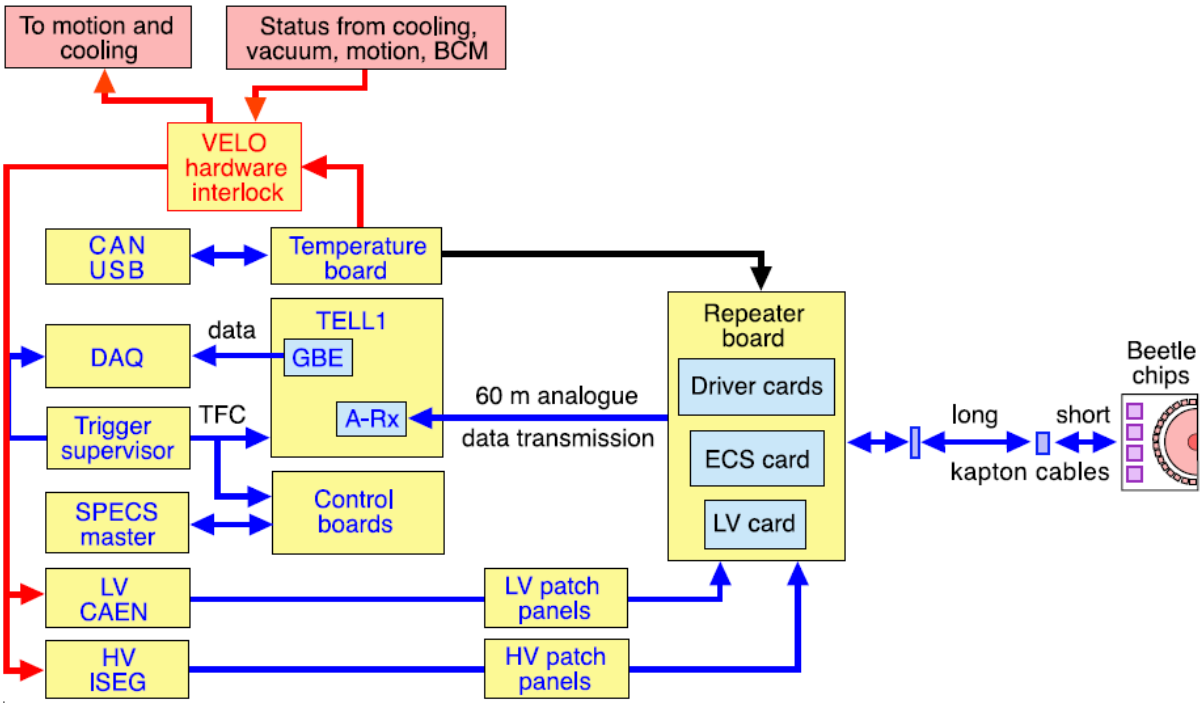

FIG. 7. LHCb VELO readout schematics at CERN. [11]

1. *Beetle Chip*

The Beetle chip is a dedicated component based on 0.25 µm CMOS technology and manages the stripes readout. The chip is equipped with 128 readout channels, one channel per stripe. The properties of a signal leaving the chip follow very stringent LHC trigger timing rules, namely, that signal raise time (between 10% and 90% of the value) is below 25 ns. Furthermore, the peak voltage remainder after 25 ns is lower than 30% for load capacitances below 35 pF, see FIG. 7.

The shaper output signal is triggered by the LHC bunch crossing. The signal charge is stored in an analogue pipeline, with a latency of 160 sampling intervals. The data from the pipeline is transferred out of the chip during a 900 ns long read out window (thus, at 1.1 MHz frequency). The data train from the pipelines is transferred along with the output signal from a so called dummy channel, which is used to compensate common mode effects induced in the chip. The technical specification of the Beetle chip can be found in TABLE III. The equivalent noise charge has been measured to be equal ENC = 497 e- + 48.3e-/pF · C_{in}.

TABLE III. Summary of the Beetle chip characteristics. [17]

Number of channels	128
Power consumption [mW/channel]	< 6.0
Peaking time [ns]	≤ 25
Pulse spill-over after 25 ns [% V_P]	< 30
Dynamic range [number of electrons]	± 110000
Required linearity [% over full range]	≤ 5
Sampling frequency [MHz]	40.0
L0 trigger rate [MHz]	1.0
Max. latency [µs] (160 x 25ns)	4.0
Readout time [ns / event]	≤ 900

2. *TELL1 board card*

Similarly to the Beetle chip, data acquisition cards were also developed for the purpose of the LHCb VELO experiment. These dedicated FPGA controlled cards consist of 64 analogue data links and perform various operations and host control systems e.g. Timing and Fast Control, Experiment Control System, L1 trigger connected to the LHC L1 trigger farm or DAQ, which connect the digitizer board to the LHCb data acquisition.

The TELL 1 board card also performs a series of operations on the analogue signal arriving from the repeater boards. In the first step the signal gets digitised with a 10-bit resolution on the ADCs at 40MHz frequency. Each ADC channel is provided with an adjustable programmable clock to compensate for different analogue signal cable lengths. Digitisation is followed by a number of several other signal processing stages, e.g.:

1. Pedestal subtraction - pedestals are determined for every single channel calculated according to Pedestal Following Algorithm. The pedestal value is set to around 512 ADC counts out of the 1024 ADC counts in the full 10-bit range (an ADC count corresponds to the signal of about 450 electrons). A variation of the pedestal value is observed from channel-to-channel, link-to-link and chip-to-chip.
2. Cross-talk removal.
3. Channel reordering – vital for further signal clustering. The electronic readout channel numbers are related to the physical sensor strip map.
4. Common mode suppression - corrects for constant shift in the signal.
5. Clustering – depending on the charge distribution between stripes surrounding the seeding strip (chosen if signal exceeds the seeding threshold – SC) A cluster is formed when signal in stripes adjacent to seeding stripe exceeds the inclusion level, see FIG. 8..

C. The LHCb VELO integration with the treatment line at CCO

In the LHCb experiment VELO hybrids operate in vacuum. The detector installation point at Clatterbridge Centre for Oncology

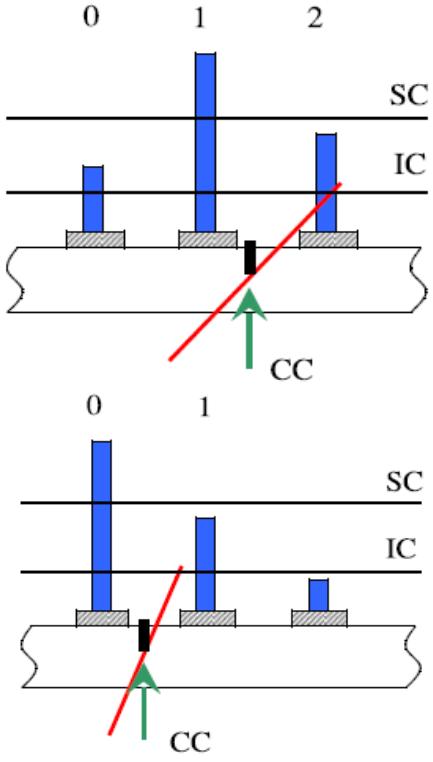

FIG. 8. Examples of clustering algorithm performed on data in TELL1 cards. Blue lines represent the charge collected from each stripe. SC and IC are respectively: seeding and inclusion thresholds. The cluster centre is depicted by black vertical bold line. Signal strength is calculated by averaging signal values. Red lines, whereas, depict the particle trajectory. [19]

anticipates its operation in air. Thus, detector integration appeared to be challenging in handling with both mechanical and thermal aspects of operation. A special emphasis was put on preventing electronics from damage due to condensation, when operating at temperatures below the dew point, and possible ice build up on cooled elements. Therefore cooling system is integrated with dry air shroud, see FIG. 9. The cooling circuit ought to dissipate the Beetle chips heat load of 40W power.

Two orthogonal translation stages, equipped with McLenan stepper motors, provide detector positioning with a resolution of 5 μm along two axes, parallel and perpendicular to the beam direction. A chiller enables the whole detector to be cooled down to -7°C, reducing noise and efficiently keeping the overall heat load down. Two perspex envelopes enclose the detector hybrids, forming dry air shrouds around the cooler elements, see Fig. 9. The required air dryer flow rate will be determined experimentally, but is expected to be lower

than the nominal flow rate of up to 45 l/min at a pressure of 8 bars.

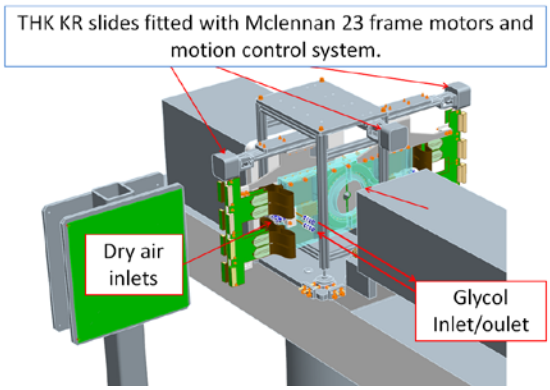

FIG. 10. Stand design to integrate the LHCb VELO detector with treatment beam line at the Clatterbridge Centre for Oncology.

ISEG EHS 82 05P-F-XXX voltage power supply is going to build the depletion region in the sensors by applying potential of up to -500V. The power supply provides stable and low noise voltage described by 5 [mVp-p] ripple at maximum load. The unit is equipped in both positive and negative polarisation channels – four of each type. Therefore both p–on-n and n-on-n type sensor hybrids can be used in the experiment.

IV. FARADAY CUP

FC is a simple and reliable device for total beam current determination. In principle, a FC is a beam stopper integrating the beam charge collected in the conductive bulky material. The material is isolated from the housing of the beam line and grounded through a charge meter.

The FC design comprised of optimising the beam stopper material and geometrical arrangement for maximising the charge collection efficiency. The studies were performed with use of FLUKA Monte Carlo transport code [14]. Both material and geometrical studies focused on proton induced fluxes of various charged particles liberated from the surface of the beam stopper under bombardment of 60MeV proton beam, corresponding to the treatment beam used at the CCO. The initial general geometrical assumptions for quantitative considerations are depicted in FIG. 10. and summarized in TABLE IV.

TABLE IV. Summary of materials and geometries tested in the FC optimisation.

Cup characteristics	
Material	Copper, Aluminium, Graphite
Cup bottom thickness [cm]	4
Inner radius [cm]	2
Outer radius [cm]	4
Well depth [cm]	6
Solid angle [sr] (polar [deg])	0.32 (~18.5)
Bottom type	Flat, Spherical, Conical
Sphere radius / Cone height [cm]	2

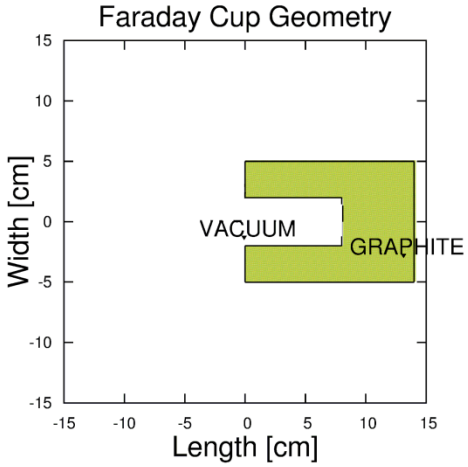

FIG. 9. Faraday Cup geometrical arrangement used for further optimisation studies.

The charge collection accuracy is a superposition of different particles fluxes and their charge, e.g.:

1. Positive charge of impinging protons fully stopped in a material gives positive contribution to the total charge collected.
2. Negative electron charge of the secondary electrons yielding from material surface gives positive contribution to charge collection.
3. Positive charge of protons: back scattered, liberated from the beam stopper surface by nuclear reactions (n, p); and charged hadrons (e.g. He-4) gives negative contribution to the charge collected.
4. Positive charge of positrons escaping from material gives negative contribution to the total charge collected.

A variety of proton interactions with matter, e.g. both inelastic proton collisions with the Fermi electron gas inside metal, or elastic collisions with the atom nuclei initiate processes, leading to generation of secondary particles spectra influencing the charge collection efficiency. Simulation studies results showed that secondary electrons and protons escaping from the metal surface cause directly accuracy deterioration. Other particles fluxes, e.g. of He-4 or positrons can be neglected and their simulations studies results are not presented in this paper.

A. Electron spectra

Ion-induced electron emission from the surface of target material contributes significantly to overall charge collection. Several different theories have been introduced over last few decades explaining the mechanisms of ion – induced electron yields and presenting various experimental results [10]. The proton 'electronic' stopping power consists of two processes: the first liberating large numbers of low-energy secondary electrons in 'distant' collisions and the latter 'close' collisions characterised by large energy transfer to small number of electrons. Proton kinetic energy transfer to electrons in close collisions can be large - enough to let them further ionise medium in cascade processes. In general, the electron emission follows the angular distribution proportional to $\cos\theta$, where θ is the emittance angle with respect to the surface normal.

Over 50% of proton – induced electrons spectra emitted from metal surface are in the low energy region of up to 50eV. This yield shows local energy maximum in region of 2 – 20eV and additionally is material dependent. However, it does not depend on the projectile energy. This mechanism is believed to be driven by cascade process of high energetic ionising δ – electrons [10]. Situation changes for emitted electron spectra in energies higher than 50eV. Than electron yield becomes impact-energy-dependent.

The mentioned high-energy electron spectrum may extend up to hundreds of keV and is believed to be triggered by inelastic proton collisions with material electrons leading to direct kinetic energy transfer [10]. The ionisation processes give raise to electron spectrum with maximum energy at about 100keV falling down for higher energies and being material and projectile dependent at the same time. It has been also shown [10] that molecular process of electron loss from the projectile may lead to electron emission at energies centred on energy corresponding to the velocity of the impinging particle. These electrons may also contribute to the lower energies spectrum and may initiate additional electron emission.

B. Proton interactions in matter

Proton kinetic energy is lost mainly in inelastic collisions with electrons whilst stopping in solid state medium. As a result, it leads to both ionisation and excitation of atoms and molecules.

The average kinetic energy lost by proton per unit distance is referred to as a 'stopping power' [MeV/(g/cm2)]. Small amounts of energy transferred in collisions with electrons lead to beam energy spread called path-length straggling (continuous slowing down approximation range – CDSA range) limiting the proton penetration depth. The alternative effect to CDSA is multiple Coulomb scattering triggered by the proton path deflections caused by atomic potential of target material nuclei. The probability of proton reversal of direction, however, is really small and furthermore decreases with energy. Nevertheless, proton range can be precisely defined and an average scattering angle in $\langle\cos\theta\rangle$ due to multiple scattering can be determined, where θ is an angle with respect to the initial proton direction at energy - E_0.

For the proton energies above 1MeV the contribution to the energy transfer in elastic nuclear collisions is less than 0.1% compared to inelastic interactions [11]. Elastic proton collisions with atomic nuclei play an important role for impact energies below 20keV [11] and are negligible for the investigated 60MeV-CCO's proton beam. Also the abrupt energy loss in non-elastic nuclear reactions is not covered in the optimisation of the FC, as they become significant for proton impact energies above 100MeV.

Other phenomenon decreasing the charge collection efficiency in the target material are the knock – on (n, p) reactions near the surface of the beam stopper. Protons can, therefore, be emitted from the surface directly into the vacuum taking their charge away.

C. Faraday cup simulations and design

The FLUKA multi – particle transport code [12] was used to estimate fluence (or current) of primary and secondary particles yielding from irradiated metal surface.

The simulation code supports charged particle transport for energies above 1keV. Thus, the low – energy electron spectra have not been simulated. Quoting, however, literature studies presented by L.J. Verhey et al. (1979), Grusell et al (1995), Cambria et al (1997), Harasimowicz (2010) a negative potential of -500 to -1000V applied to a guarding ring located at the entrance of the FC effectively suppresses low energy electrons yielding from the surface of the beam stopper. Moreover it also creates a guarding potential for tertiary electrons yielding from the vacuum widow (Kapton).

The tertiary electrons energy spectrum can be easily estimated on the basis of the Binary Encounter Peak [10]. The energy transfer to a quasi – free electron of mass m_e from a fast heavy projectile of mass M_p and total energy transferred to medium E_p can be estimated according to the following formula:

$$E_{BEA} \approx \frac{4m_e}{M_p} \cdot E_p \cdot \cos^2\theta$$

where θ is the scattering angle of the electron with respect to the direction of the impinging projectile. The maximum energy transferred to electrons is obtained by those emitted in the forward direction of the projectile ($\theta = 0$). The electron energy depends on both the material type and thickness.

FULKA simulation studies on FC optimisation considered three different materials and beam stopper arrangements according to the summary in TABLE V. The depth of the beam stopper was chosen to increase the charge collection efficiency by decreasing the particle emission solid angle. The solid angle was set to 0.32 sr, what corresponds to approx. 18.5 degrees in polar angle. Three different shapes of target surface were tested: plane, cone and sphere. Various target shapes were tested to find optimum between ion-induced particles spectra and spatial distribution (which in the end were the only criterion) and alternative heat dissipation in material, even though no special thermal energy dissipation treatment is required [15] as the beam power is estimated to be $P = 0.3\ [W]$.

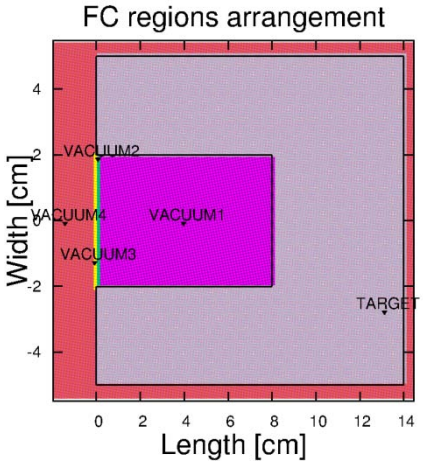

FIG. 11. Region arrangement in the simulation for estimating the ion-induced particle currents leaving the Faraday cup, thus, influencing the charge collection efficiency.

A FLUKA built-in boundary crossing estimator - USRBDX - was used to estimate the current of ion – induced emission particles, e.g. protons, electrons, positrons, He-4 (based on FLUKA output file) and photons spectrum. The average fluence through a surface S of infinitesimal thickness dt may be estimated according to the formula:

$$\Phi = \lim_{dt \to 0} \frac{\sum_i \frac{dt}{\cos\theta_i}}{S\ dt}$$

where θ is incident particle angle with respect to the normal of the surface. The USRBDX estimation was set at four different boundaries between adjacent regions, see FIG. 11, e.g. Target to Vacuum 1 or Vacuum 3 to Vacuum 4.

FLUKA input file contained different variables defining i.e. particle transport options, particles production thresholds and physics phenomena, and they are briefly summarized in TABLE V.

TABLE V. FLUKA input file variables used in FC optimisation.

Beam parameters		
Particle type		p
Particle kinetic energy [MeV]		60
Beam shape		Annular
Number of particles		3.12 *e* 10
Transport options		
Electromagnetic interactions	Electrons / positrons	
	Kinetic energy threshold [keV]	1.0
	Phenomena	Bremsstrahlung, pair production, photoelectric effect
	Electromagnetic radiation	
	Transport energy threshold [keV]	0.1
Proton transport threshold [keV]		0.1
Multiple Coulomb Scattering		Enabled
Neutron transport and self-shielding		Enabled

D. Simulation results

3. Material considerations

Ion-induced secondary particles currents were estimated with FLUKA for three different materials: copper, aluminium and graphite.

Simulation results agree with theoretical predictions in terms of current and energy spectra of secondary charged particles: electrons and protons.

FIG. 12 illustrates proton double differential fluence $d^2f/dE\,d\Omega$ (depicted on the plot as a function of polar angle with respect to the surface normal) for aluminium beam stopper. Number of protons emitted in the reverse direction at energies around 60MeV is small due to very low probability of elastic proton scattering on the target nuclei. In contrast, however, the low energy spectra are sharp and well visible. In order to obtain the total particle current of one type, the integration over energy and angle was performed. Integration results related to the actual treatment beam current at CCO of $I_b = 5\ nA$ show that the charge loss is smaller than 0.1% for all three materials taken into

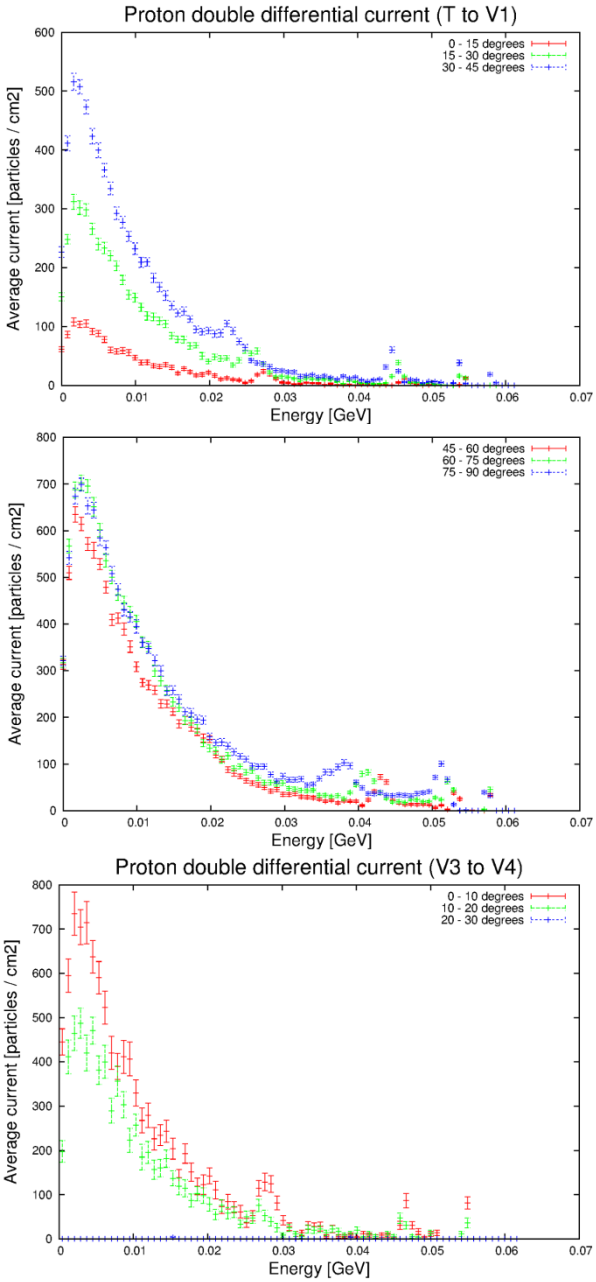

FIG. 12. Proton double differential current spectrum for Aluminum with respect to energy and angle. First two top plots depict proton fluence assessed with USRBDX estimator liberated from the target material to the vacuum 1 region. The third bottom plot illustrates the proton fluence between two vaccum regions V3 - V4. Flunece demonstrates siginificant reduction limited solid angle emission cone.

consideration (summarised in TABLES VI to IX).

TABLE VI. Total proton current estimation between regions Target to Vacuum 1.

Material	I [nA]	$I_{\%}$	ΔI [nA]	$\Delta I_{\%}$
Copper	$3.35 \cdot 10^{-3}$	0.08	$2.97 \cdot 10^{-5}$	< 0.01
Aluminium	$2.57 \cdot 10^{-3}$	0.06	$2.54 \cdot 10^{-5}$	< 0.01
Graphite	$1.69 \cdot 10^{-3}$	0.04	$2.54 \cdot 10^{-5}$	< 0.01

TABLE VII. Total proton current estimation between regions Vacuum 3 to Vacuum 4 (leaving the system).

Material	I [nA]	$I_{\%}$	ΔI [nA]	$\Delta I_{\%}$
Copper	$1.00 \cdot 10^{-4}$	0.002	$3.28 \cdot 10^{-6}$	< 0.001
Aluminium	$7.66 \cdot 10^{-5}$	0.002	$2.85 \cdot 10^{-6}$	< 0.001
Graphite	$3.55 \cdot 10^{-5}$	0.001	$2.28 \cdot 10^{-6}$	< 0.001

TABLE VIII. Total electron current estimation between regions Target to Vacuum 1.

Material	I [nA]	$I_{\%}$	ΔI [nA]	$\Delta I_{\%}$
Copper	$4.83 \cdot 10^{-3}$	0.11	$3.35 \cdot 10^{-4}$	0.004
Aluminium	$2.20 \cdot 10^{-3}$	0.05	$2.14 \cdot 10^{-4}$	0.001
Graphite	$4.36 \cdot 10^{-4}$	0.01	$1.09 \cdot 10^{-4}$	< 0.001

TABLE IX. Total electron current estimation between regions Vacuum 3 and Vacuum 4 (leaving the system).

Material	I [nA]	$I_{\%}$	ΔI [nA]	$\Delta I_{\%}$
Copper	$5{,}45 \cdot 10^{-4}$	0.011	$1.24 \cdot 10^{-5}$	0.001
Aluminium	$3.22 \cdot 10^{-4}$	0.007	$9.14 \cdot 10^{-6}$	< 0.001
Graphite	$3.38 \cdot 10^{-5}$	0.001	$5.04 \cdot 10^{-6}$	< 0.001

Electron double differential current spectrum with respect to the energy and solid angle (corresponding to the polar angle) yielding from the surface of aluminium target are presented in FIG. 13. Fraction of the electrons escaping to the vacuum and taking the charge away is plotted in FIG. 14 (boundary crossing estimation between regions Vacuum 3 and Vacuum 4). As can be easily noticed, the maximum electron energies do not exceed the impinging protons maximum kinetic energy. Moreover, results agree with theoretical predictions of molecular effects i.e. electron loss by projectile. The electron energy spectrum is continuous as expected. Electrons loose part of their kinetic energy drifting towards the surface in different interactions e.g. multiple ionisation effects or path deflections; thus, contributing to the continuous spectrum.

The obtained results also show the dependence of electron emission from surface on material type. As predicted, copper demonstrates highest electron yield decreasing gradually when shifting to lighter material – aluminium - and the lightest compound - graphite. It has been already mentioned that the charge collection efficiency is influenced by fluence of different type of particles.

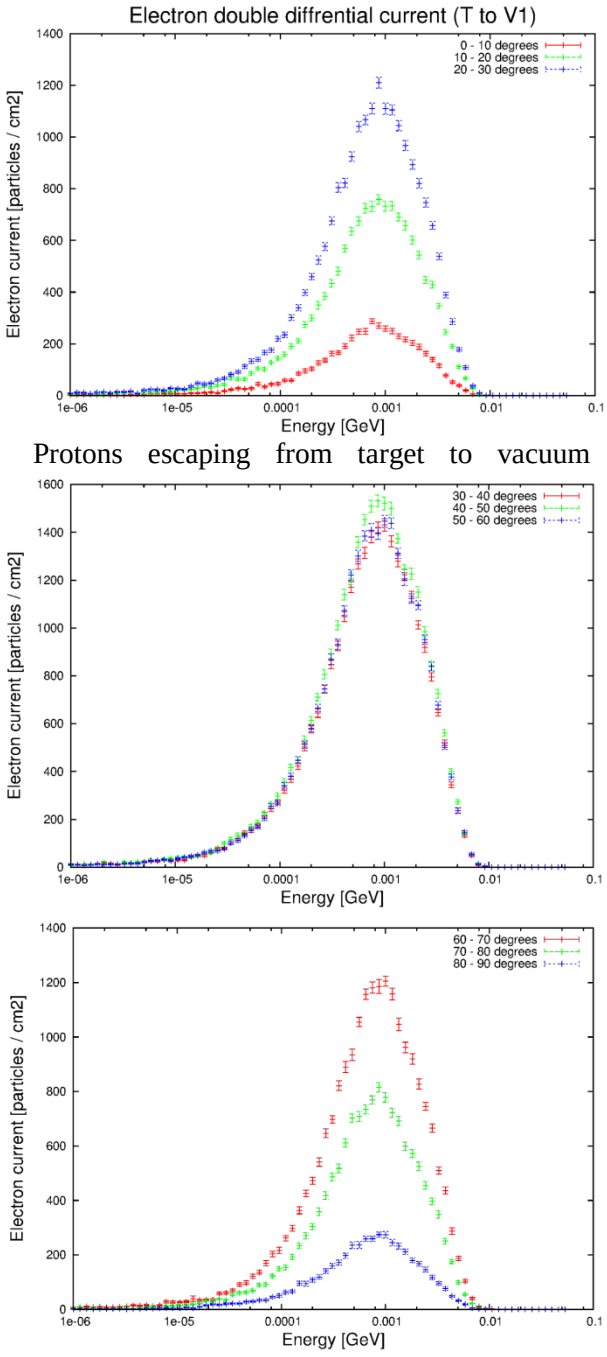

FIG. 13. Double differential proton fluence on boundary crossing between regions Target and Vacuum 1.

Protons escaping from target to vacuum negatively affect collected charge by decreasing the current value. At the same time

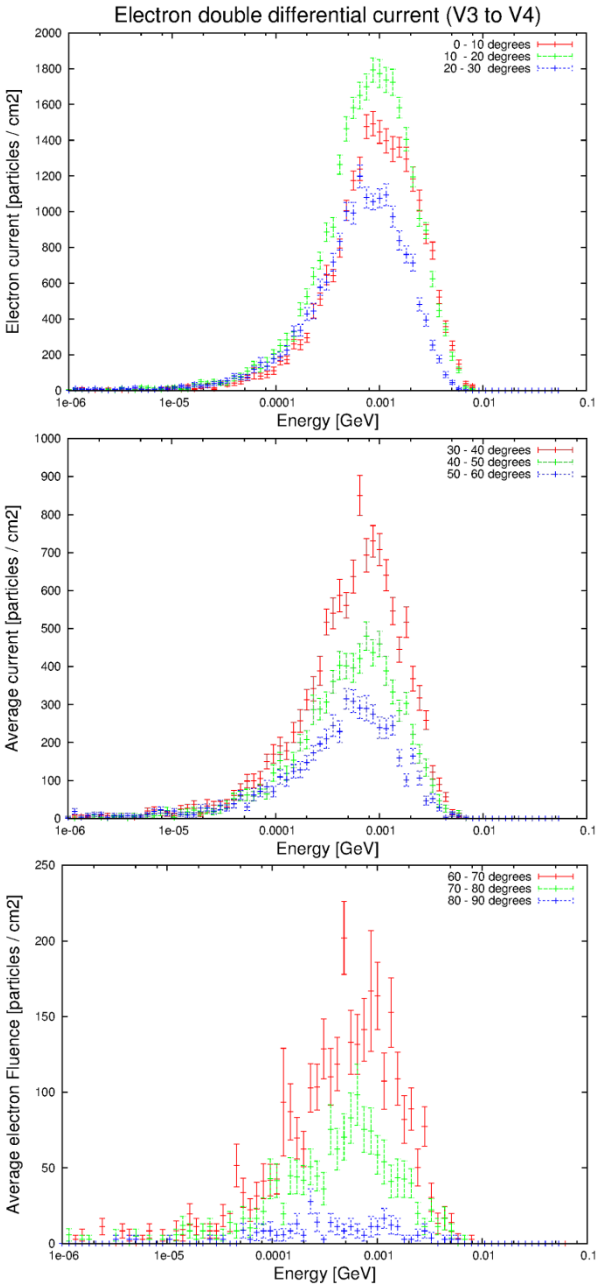

FIG. 14. Electron current estimated on boundary crossing between vacuum 3 and vacuum 4 regions (leaving the cup). Geometrical arrangement decreases the charge loss for electrons emitted for angles over 18.5 deg.

ion–induced electron flux in the same direction increases the actual current value. Total electron current obtained by integration of electron current double differential distribution over energy and solid angle shows that relative signal increase of actual proton beam current $I_b = 5\ nA$ at CCO for three assessed materials are respectively: approx. 0.01% for copper, 0.005% for aluminium and less than 0.001% for graphite. The calculations do not show, however, quantitative particle fluxes from the outer surface of the beam stopper to the vacuum, caused by distant neutron induced knock–on reactions. The qualitative assessment in FLUKA showed however that they can be neglected.

4. Geometrical considerations

Flat, conical and spherical target surface was used to estimate the ion-induced particles currents, see TABLE IV. Treatment beam power does not require any special thermal treatment of the FC beam stopper. The decision on the target shape was thus made finding the minimum between the signal deterioration and lowest production cost and the sake of manufacturing simplicity. Simulation results for proton and electron currents originating from the graphite target surface are summarised in TABLE X and TABLE XI.

TABLE X. Proton current from graphite target for different target bottom shapes: flat, spherical and conical geometries.

Tested geometry	I [nA]	ΔI [nA]
Flat	$4{,}76 \cdot 10^{-5}$	$5.57 \cdot 10^{-6}$
Spherical	$5.72 \cdot 10^{-5}$	$6.31 \cdot 10^{-6}$
Conical	$6.07 \cdot 10^{-5}$	$6.42 \cdot 10^{-6}$

TABLE XI. Electron current for graphite target for different target bottom shapes: flat, spherical and conical geometry.

Tested geometry	I [nA]	ΔI [nA]
Flat	$2.66 \cdot 10^{-4}$	$2.34 \cdot 10^{-6}$
Spherical	$2.81 \cdot 10^{-4}$	$2.40 \cdot 10^{-6}$
Conical	$2.67 \cdot 10^{-4}$	$2.42 \cdot 10^{-6}$

The estimated ion – induced electron or proton current leaving the target material as a function of the target shape does not show any significant difference within the estimated uncertainty. Ultimately, a flat target shape was chosen to reduce the cost of manufacturing.

V. OUTLOOK

A test stand was designed to allow for the integration of the LHCb VELO detector into the treatment beam line at the Clatterbridge Centre for Oncology. There, the detector will be used as a new online, non–intrusive beam

monitor, based on proton beam 'halo' detection. Particular challenges were to guarantee the possibility of moving the detector remotely, as well as to include an efficient cooling system to avoid over-heating and minimizing noise. This system is presently being assembled and will allow installing the apparatus in a free space region in proximity of the patient.

Aluminium based FC was also designed and optimised for the characteristics of the proton beam at CCO and will be used to precisely determine the absolute beam current. The LHCb VELO readings will then be related to the current readings and studies will be carried out to determine the sensitivity and reliability of signal cross correlation. Thereby, halo signal-dose mappings shall be determined to allow for a true online monitoring system during patient treatment. The shape of the FC beam stopper has been optimised in numerical simulations with FLUKA. The stopper will be built from Aluminium since it showed lower proton-induced particles emission than copper and it can be machined much easier than graphite. The readout electronics for the FC will be proposed shortly and custom made software is being developed to read out and analyse the VELO and FC data simultaneously.

VI. REFERENCES

1. Technical Report Series No. 398: 'Absorbed Dose Determination in External Beam Radiotherapy', International Atomic Energy Agency, Vienna 2000
2. E.B. Podgorsak, 'Radiation Oncology Physics: A Handbook for Teachers and Students', International Atomic Energy Agency, Vienna 2005
3. Thomas F. DeLaney, Hanne M. Kooy, 'Proton charged particle radiotherapy', Lippincott Williams & Wilkins, Philadelphia 2008
4. Wioletta Wieszczycka, Waldemar Scharf, 'Proton Radiotherapy Accelerators', World Scientific Publishing Co. Pte. Ltd., Singapore 2001
5. ICRU Report No. 49, 'Stopping Powers and Ranges for Protons and Alpha Particles', ICRU 1993.
6. A. Kacperek, 'Proton therapy of eye tumours in the UK: a review of the treatment at Clatterbridge, Applied Radiation and Isotopes 67, 378-386 (2009)
7. W. Kleeven, 'Injection and extraction from cyclotrons', CAS-CERN Accelerator Schooland KVI: Specialised CAS Course on Small Accelerators, CERN-2006-012, Geneva 2006
8. G. Casse et al., ' A LHCb VELO module as beam quality monitor for proton therapy beam at the Clatterbridge Centre for Oncology', Liverpool 2010
9. The LHCb Technical Design Report, Re-optimized Detector Design and Performance, LHCb TDR 9, CERN, Geneva 2003
10. D. Hasselkamp et al., 'Particle Induced Electron Emission II', Springer-Verlag Berlin Heidelberg 1992
11. J.F. Janni et al., 'Proton Range – Energy Tables, 1keV – 10GeV: Energy Loss, Range, Path Length, Time-of-Flight, Straggling, Multiple Scattering, and Nuclear Interaction Probability', Atomic Data and Nuclear Data Tables No. 27, 147-339 (1982)
12. L. J. Verhey et al., 'The Determination of Absorbed Dose in a Proton Beam for Purposes of Charged – Particle Radiation Therapy', Radiation Research No. 79, 34-54 (1979)
13. E. Grusell et al., 'Faraday cup dosimetry in a proton therapy beam without collimation', Phys. Med. Biol. 40, 1831 (1995)
14. A. Ferrari et al. 'FLUKA: a multi-particle transport code', CERN-2005-010, CERN, Geneva 2005
15. P. Strehl, 'Beam Instrumentation and Diagnostics', Springer-Verlag Berlin Heidelberg 2006
16. LHCb VELO Technical Design Report, CERN/LHCC 2001-0011, LHCb TDR 5, Geneva
17. The LHCb Detector at LHC, Journal of Instrumentation, Institute of Physics, 2008
18. S. Loechner, M. Schmelling, The Beetle Reference Manual - chip version 1.3, 1.4 and 1.5, LHCb-2005-105, CERN, Geneva 2006
19. T. Szumlak, C. Parkes, Application of the Pedestal Following Algorithm to the VELO Detector, LHCb-2009-036, CERN, Geneva 2009

20. T. Szumlak et al., Reconstruction of Cluster Positions in the LHCb VELO, LHCb-2007-151, CERN, Geneva 2007
21. A. Bates et al., VELO module characterisation: Results from the Glasgow LHCb VELO module burn-in, Glasgow 2007